JOURNAL OF AIRCRAFT
Vol. 39, No. 5, September–October 2002

Numerical Investigation of Slat and Compressibility Effects for a High-Lift Wing

M. David Baker,* Donovan L. Mathias,† and Karlin R. Roth‡
NASA Ames Research Center, Moffett Field, California 94035
and
Russell M. Cummings§
California Polytechnic State University, San Luis Obispo, California 93407

Three-dimensional multielement wings are simulated to investigate slat aerodynamics, numerical modeling techniques, and compressibility effects for high-lift flows. The computations are performed by solving both the incompressible and compressible Navier–Stokes equations on structured, overset grids. Turbulence is modeled via the one-equation Spalart–Allmaras model. All of the computed cases include the main wing with a half-span flap deflected to 40 deg. Three leading-edge configurations of this unswept wing are then considered: no slat, full-span slat, and a three-quarter-span slat. The slat elements are deployed to 6 deg. Computations of the model, which simulates a landing configuration at 10-deg angle of attack and a chord-based Reynolds number of 3.7×10^6, are validated with surface pressure measurements acquired at the NASA Ames 7- by 10-Foot Wind Tunnel. By the observation of the changes to the high-lift flowfield by adding the slat, as well as by varying its spanwise length, a detailed computational assessment of a properly configured slat is achieved. Moreover, the results increase the computational knowledge of how to model the slat flow physics accurately. For the three-element wing with part-span slat, modeling compressibility can have a large impact on the flowfield solution. Overall, compressibility is small, but it has significant global effects on the circulation and flow separation of each element.

Introduction

ONE current challenge for computational fluid dynamics (CFD) research is the accurate prediction of high-lift flows. In contrast to cruise configurations where the wing consists of a single, simply connected geometry, typical high-lift systems for both transports and military aircraft employ both leading-edge devices (such as slats) and trailing-edge devices (such as slotted flaps) that are separated from the main wing element by very small gaps. For realistic three-dimensional configurations, these devices often extend only partially across the span and lie in close proximity to structural elements such as supporting brackets, engines, and pylons.

The high-lift system also introduces complex flow physics. In his classic 1974 lecture, Smith describes the effects of the lifting performance of multiple-element airfoils with properly designed gaps.[1] Many of these concepts can be illustrated using potential flow relationships between the elements of the high-lift airfoil. Nevertheless, high-lift system performance is dominated by viscous effects. Meredith enumerates some of the viscous phenomena for multielement airfoils: 1) boundary-layer transition, 2) shock and boundary-layer interaction, 3) viscous wake interactions, 4) confluent wakes and boundary layers, and 5) flow separation.[2] Each of these viscous flow phenomena pose extreme difficulties for CFD modeling.

Many two-dimensional viscous Navier–Stokes simulations of the flow over multielement airfoils have been reported. These studies range from the early work by Shuster and Birckelbaw[3] to recent studies by Rumsey et al.[4] and Fejtek.[5] Rumsey et al.[4] investigated the flow over two different multielement airfoils. They concluded that specification of transition location is crucial to the accurate computation of boundary-layer profiles, that the prediction of the slat flowfield is difficult, and that the performance of eddy viscosity turbulence models and a nonlinear explicit algebraic stress model are similar for this flow. Fejtek[5] surveyed the results of a code validation challenge sponsored by the CFD Society of Canada; the test case was a three-element airfoil configured for takeoff.

Because of geometric and physical complexities, as well as the associated intense resource requirements for high-lift CFD, reports on three-dimensional Navier–Stokes applications are limited. In 1993, Rogers[6] demonstrated overset grid techniques for the main wing and flap elements of a T-39 Sabreliner aircraft, although the grid density was too coarse to resolve the flowfield properly. The following year, Mathias[7] and Mathias et al.[8] computed the flow about a two-element, unswept wing with a part-span flap using an incompressible Navier–Stokes code. The computations captured the flow near the flap edge and compared favorably with experimental data. From 1995 to the present, similar viscous computations for unswept, two-element wings with part-span flaps have been reported by Jones et al.,[9] who also used an overset approach; by Khorrami et al.,[10,11] who applied a patched grid approach and focused on the airframe noise aspects of the flow, and by Mavriplis and Venkatakrishnan[12] and Anderson et al.,[13] who investigated unstructured grid approaches. Recent investigations have addressed more realistic high-lift geometries. For example, Rogers et al.[14] applied and evaluated the overset grid method for a Boeing 747PD high-lift configuration.

This study extends the previous three-dimensional, high-lift CFD research in two ways. First, a slat element is added to the unswept, two-element wing geometry simulated by Mathias et al.[8] Two configurations, which include a full-span and a three-quarter-span slat, are computed to quantify the impact of slat aerodynamics to the computed high-lift flowfield. These computations address three-dimensional characteristics of the flow that can drastically change with the inclusion of slats of various length. Furthermore, these computations give quantifiable results and reaffirm existing physical insight.

Received 16 June 2000; revision received 15 March 2002; accepted for publication 9 April 2002.

*Research Scientist, Integrated Systems Technology Branch, MCAT, Inc.
†Aerospace Engineer, Systems Analysis Branch. Senior Member AIAA.
‡Chief, Aerospace Operations Modeling Office. Associate Fellow AIAA.
§Professor, Aerospace Engineering Department. Associate Fellow AIAA.

Second, by studying the unswept, three-element wing geometry, which is relatively simple in comparison to a complete aircraft high-lift system, some limited numerical investigations can be conducted for the first time in three dimensions. Assessing the effects of compressibility of the three-element wing with part-span slat required comparisons between compressible and incompressible solutions. It was found that minor variations in numerical parameters produced results that differed more than the effects due to compressibility. Various solution methods are investigated that show significant impacts on the accuracy of the high-lift flowfield computations.

This paper contains a description of the high-lift wing geometries with part-span slat and flap elements. A brief description of the INS3D and OVERFLOW algorithms is provided; this description focuses on stating the numerical parameters selected for the simulations. Complete details of the computational grid systems and numerical boundary conditions are given. The results are presented in three sections: a solution accuracy study that addresses convergence criteria and tunnel calibration, a numerical study of slat aerodynamics including experimental validation, and an assessment of compressibility effects and numerical modeling parameters based on code-to-code comparisons. Finally, conclusions are made.

High-Lift Wing Geometry

The baseline wing for this investigation consists of a NACA 63_2-215 Model B airfoil section.[15] Figure 1 shows the rigging of the complete three-element section. The reference chord length c for the unflapped section of the wing is 30 in (76.2 cm). Across one-half of the span, a 30% chord Fowler flap was installed. The flap was deflected 40 deg with a gap of 2.6% chord and an overlap of 1.5% chord. To quantify the influence of a slat, three different leading-edge configurations were investigated: a two-element wing without a slat, a three-element wing with a full-span slat, and a three-element wing with a three-quarter span slat. Both the full-span and part-span slats were deflected 6 deg and deployed to a gap of 2.0% chord and an overlap of -0.5% chord.

These configurations were experimentally studied by Storms et al.[16] in a series of tests conducted in the NASA Ames Research Center 7-by-10-Foot Wind Tunnel. The model vertically spanned the tunnel between two splitter-plate walls, thereby reducing the effective test section size to 5 by 10 ft (1.524 by 3.048 m), or 2 chords by 4 chords. The experimental repeatability of total lift coefficient was ± 0.01 for an actual C_L less than or equal to $0.95C_{L\,\max}$. The total lift coefficient was based on integration of pressure measurements. The pressure measurements were made with pressure transducers having different accuracy ranges: 0.31% for $C_p > -1$, 0.28% for $-1 > C_p > -2$, 0.26% for $-2 > C_p > -5$, and 0.21% for $C_p < -5$. Because the majority of pressure coefficients measured were between $C_p = 1$ and -3, the average uncertainty is approximately 0.30%. Figure 2 shows a planform view of the model and the spanwise locations where surface pressure measurements were acquired. The wing span b equals two chord lengths. Trip disks were placed at $0.05c$ and $0.10c$ on the upper and lower surfaces of the main element, respectively, for the two-element wing without a slat. No trip disks were used on the three-element configurations in the experimental tests.

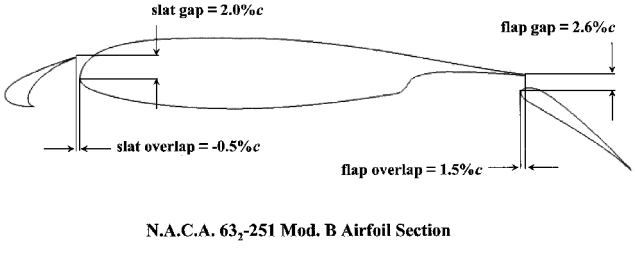

Fig. 1 Position of the slat and flap elements for the two- and three-element wings.

Table 1 Mach number and exit boundary condition comparisons for the tunnel calibration study

Code	M_∞	Exit boundary condition
OVERFLOW	0.22	Exit extrapolation with fixed static pressure
OVERFLOW	0.22	Specified exit mass flow ratio
OVERFLOW	0.22	Exit extrapolation of all variables
INS3D	N/A	Exit extrapolation with fixed static pressure

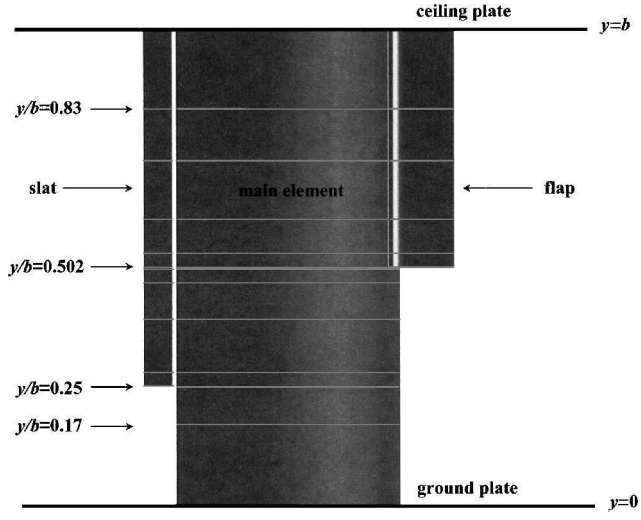

Fig. 2 Experimental spanwise pressure tap locations for the two- and three-element wings (locations are defined where computational results are presented).

Numerical Approach

All of the computations were performed using the experimental coordinate system with the wing positioned at 10-deg angle of attack and at a chord-based Reynolds number of 3.7×10^6. The tunnel was modeled according to the experimental test section dimensions (2 chords $\times$ 4 chords). The inlet and outlet planes of the tunnel were placed 10 chords upstream and 10 chords downstream of the model, respectively. A Mach number of 0.22 was used for the slat aerodynamics study. Table 1 describes Mach number and specific code features for the tunnel calibration study and compressibility effects study.

Algorithm and Turbulence Model Selection

Compressible Flow Solver

Most simulations were conducted using the compressible Navier–Stokes code OVERFLOW.[17,18] This code was selected for application because it computes solutions on overset grid systems, a technique that has been shown to be effective for the geometric complexities associated with high-lift configurations.[14] The numerical method is based on the alternating direction implicit Beam–Warming approximate factorization scheme.[19] The code employs central differencing for the left-hand side terms in all spatial directions with added second- and fourth-order artificial smoothing for stability.[20] The right-hand side spatial differencing for the convective fluxes is performed with a third-order upwind scheme based on Roe's flux differencing method.[21] The right-hand side spatial differencing for the viscous fluxes is performed via central differencing.

Each OVERFLOW case was run using a time step of 0.1, a minimum Courant–Friedrichs–Lewy (CFL) number cutoff for the locally varying time stepping of 5.0, a minimum CFL number for the turbulence model of 4.0, and the multigrid option for convergence acceleration.[17] In addition, thin-layer and viscous cross terms were retained in each computational direction to achieve fully viscous conditions. Low Mach preconditioning was also used for selected cases in the compressibility study, as is shown in Table 2.

Table 2 Mach number and algorithm enhancements used for compressibility effects study

Code	M_∞	Solver acceleration
OVERFLOW	0.22	——
OVERFLOW	0.22	LMP
OVERFLOW	0.001	LMP
INS3D	N/A	——

Incompressible Flow Solver

An incompressible solution for the compressibility study was generated using the INS3D-UP code[22]; this code also relies on the structured, overset grid methodology. The INS3D solver uses a block Gauss–Seidel iterative method that employs a line-relaxation scheme, which allows for very large pseudotime steps enabling fast convergence for steady-state flow problems. Spatial differencing on the convective terms is done through the use of the method of artificial compressibility and third-order upwind flux differencing that is also based on Roe's scheme.[21] Viscous flux terms are spatially differenced using second-order central differencing. The INS3D solution was run using a artificial compressibility parameter that sets the wave speed β to 100.

Turbulence Modeling

The results of previous two- and three-dimensional high-lift CFD studies[4,14,23–25] suggest that the one-equation Spalart–Allmaras[26] turbulence model is currently the most appropriate eddy viscosity model for high-lift flows in terms of accuracy and efficiency; it was used to model the eddy viscosity in all of the simulations. The current implementation of the model within each flow solver did not allow for laminar–turbulent transition of the flow, so that all of the calculations assume a fully turbulent flow over the wing. Even though the Reynolds numbers are relatively low, valid comparisons with the experimental data can be made due to the boundary-layer tripping of the two-element wing and rapid free transition likely to occur on the three-element wings.

Domain Discretization

Overset Grid Generation

Structured, overset grids are used throughout this study. The grid generation is similar to the approach taken by Mathias[7] and Mathias et al.,[8] who established the necessary spanwise and streamwise grid resolution for the flowfield with the two-element wing. Moreover, the grid generation makes extensive use of the Chimera Grid Tools package[27] and the hyperbolic grid generator, HYPGEN, which was used for each component volume grid.[28] Grids for the two-element wing and the three-element wing with full-span slat are essentially a subset of the grid system for the three-element wing with part-span slat. For the two-element wing, the slat grids are removed. For the three-element wing with full-span slat, the slat-tip grid is removed and additional planes are added in the spanwise direction. Details about grid topology and grid size are presented in Ref. 29.

All of the wing-surface zones were embedded in a far-field box grid representing the effective wind-tunnel test section. The test section geometry was extended 10 chord lengths upstream and downstream from the leading edge of the main wing element and used inviscid spacing. The individual grid zones were merged using the PEGSUS code.[30] The composite mesh contains 3.94 million points within eight zones. Mesh sizes for the two-element case and the full-span slat case are 2.31 million points and 3.02 million points, respectively.

Boundary Conditions

To enable code-to-code comparisons between the OVERFLOW and INS3D solvers, the same computational boundary conditions were invoked in both codes. All of the solid surfaces on the high-lift wing were modeled using an adiabatic viscous wall boundary condition, which specified zero velocity and zero normal pressure gradient at the surface point. A C-grid flow-through condition, which averages quantities from the points above and below the wake boundaries, was applied along the wake boundaries of the slat, main wing, and flap zones. This boundary condition was also applied to the wake-extension portions of the slat cap. The partial fold-over axes for the slat cap were specified using an axis condition that imposes the average value of the immediately surrounding nodes onto the axis point.

The wind-tunnel walls were treated inviscidly in both codes by imposing a zero normal gradient of the velocity at the wall nodes. For the INS3D solution, uniform normal velocity and total pressure were prescribed at the tunnel inlet. At the tunnel exit, a constant static pressure was prescribed with the velocity field extrapolated from the grid plane immediately preceding the exit plane. These conditions were previously validated by Mathias[7] and Mathias et al.[8]

Solution Accuracy

Convergence Criteria

Both the L_2 norm of the residuals and the total lift and drag coefficients were monitored to determine convergence for the OVERFLOW simulations. For these steady-state, high-lift computations, an acceptable level of convergence was reached when the L_2 norm for each of the computational grids had dropped by three orders of magnitude. In addition, the variation in the total lift coefficient was required to be within 20 counts (1 count = 0.0001) for the last 100 cycles, which is two orders of magnitude more accurate than the experimental data. Typical convergence histories for all cases are shown in Figs. 3a and 3b. Figures 3 show the L_2 norm and total lift vs computational cycle for the part-span slat solution used in the compressibility study (where the freestream Mach number was 0.001 and low Mach preconditioning was implemented). Convergence required about 2500 multigrid cycles for most cases; the part-span slat case required about 280 h of CRAY J90 CPU h, which roughly equals 65 CPU h for a CRAY C90.

Convergence for the INS3D solution was dictated by the order of magnitude of the divergence, which is a measure of mass conservation. Iterations were terminated once the maximum value of the divergence parameter at any location within the composite mesh was at or below unity. The maximum value of the divergence was located at a chimera boundary of two overlapping zones; achieving a lower level of divergence in this case would have been impractical and probably would not have changed the solution to any detectable degree. Convergence of the part-span slat configuration using INS3D required approximately 265 CRAY J90 h for nearly 700 cycles.

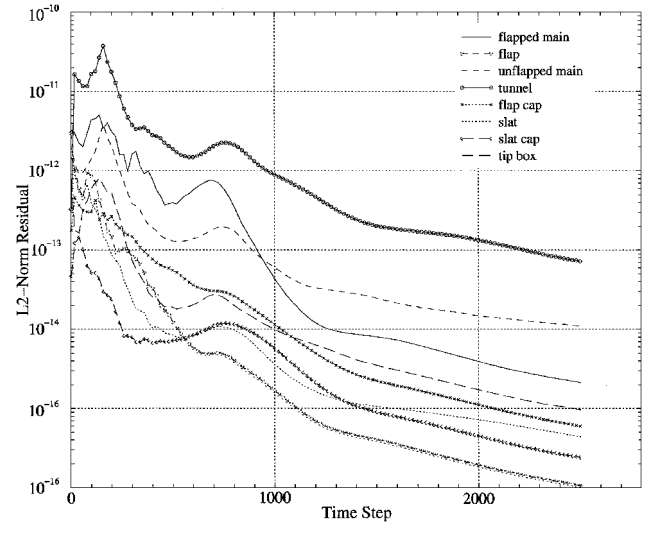

Fig. 3a L_2 norm residual convergence history for OVERFLOW solutions; three-element part-span slat wing.

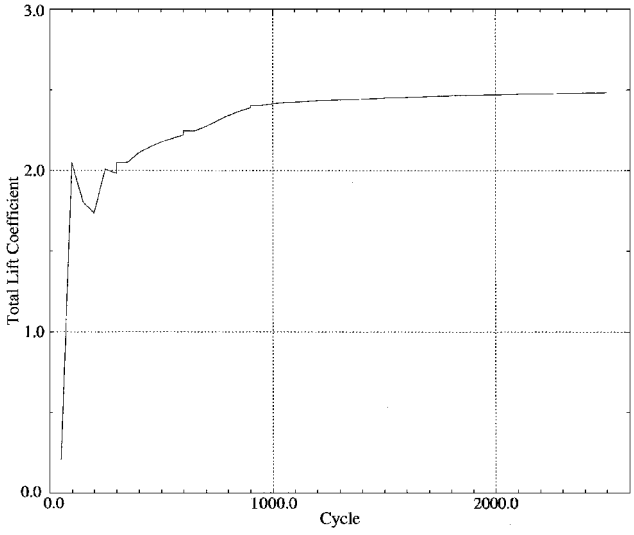

Fig. 3b Total lift coefficient convergence history for OVERFLOW solutions; three-element part-span slat wing.

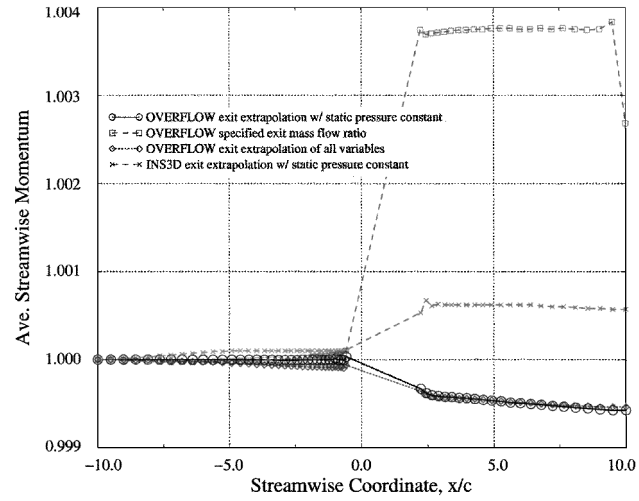

Fig. 4a Wind-tunnel test section conditions calibration comparing averaged momentum flux using various exit boundary conditions for compressible and incompressible solutions.

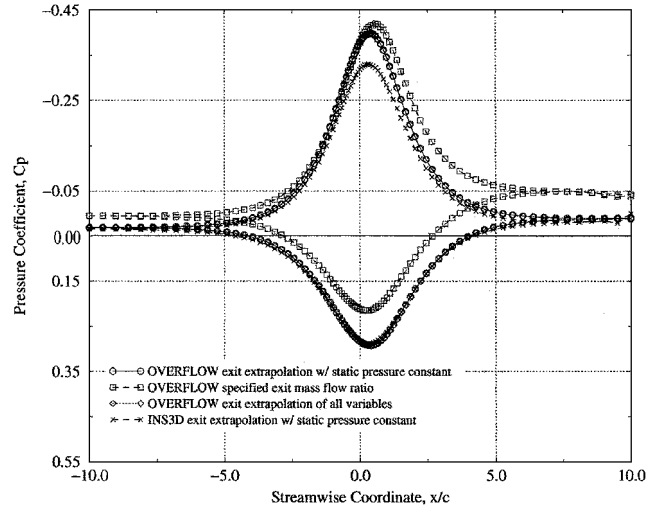

Fig. 4b Wind-tunnel test section conditions calibration comparing pressure distributions on tunnel side walls using various exit boundary conditions for compressible and incompressible solutions.

Tunnel Calibration

From a numerical point of view, a primary objective of a tunnel simulation is to achieve a flow solution in the test section similar to the tunnel operation condition.[31] Attention needs to be placed on boundary conditions when attempting to compare the results of experiments and numerical modeling. Improper pressure or velocity conditions at a tunnel exit plane, for instance, can induce the incorrect velocity condition at the test section, or even introduce reflective pressure waves that can inhibit the convergence rate of the solution.[31] For the purposes of a compressibility study, similar flow conditions must be achieved at the test section for the compressible and incompressible numerical simulations.

The internal flow problem of this study required a calibration of the outflow boundary condition for the solutions computed with the OVERFLOW code. Mathias had found little effect on the flow by varying the outflow conditions in INS3D between extrapolation and characteristic conditions in his study.[7] Furthermore, because the INS3D results in this study and in the Mathias[7] and Mathias et al. results[8] agreed well with experiment, effort was placed in calibrating the OVERFLOW solutions in reference to the INS3D solutions. Surveys of the flow within the wind-tunnel test section with the test article installed were not made in the experiment.

Three OVERFLOW outflow boundary conditions were investigated and are shown in Table 1. The outflow boundary condition that prescribed a constant static pressure at the exit was finally used. Similar to the INS3D outflow condition, the velocity field and other flow quantities are extrapolated from the preceding grid plane. The initial approaches to the compressibility study used the specified tunnel exit mass flow condition. This boundary condition was developed by Djomheri[31] as a convergence enhancement for internal simulations of the NASA 12-Foot Pressure Wind Tunnel. A physical interpretation of this boundary condition is based on global conservation of mass in the tunnel. This boundary condition assumes the variation of flow velocity normal to the tunnel exit plane is small. A third exit condition available in OVERFLOW, which extrapolated all flow variables at the tunnel exit, was also considered.

Figure 4a shows the averaged, normalized momentum flux throughout the tunnel for three OVERFLOW simulations and the INS3D simulation with different exit conditions. The high-lift wing is configured with the part-span slat in each case. The straight-line segments near $x/c = 0$ on the curves represents the location of the high-lift model, where the tunnel grid points have been cut away or blanked out by the PEGSUS interpolation scheme.[30] The onset momentum is fairly equivalent between the solutions, as shown in Fig. 4a. Conversely, the momentum flux aft of the test section region varies significantly over the different solutions. The OVERFLOW solution using the specified mass flow ratio exit condition causes a large increase in momentum aft of the high-lift wing. At this location, the OVERFLOW solutions using the extrapolation conditions show a slightly lower momentum loss aft of the test section than does the INS3D solution using an extrapolation condition.

Although the scale of the averaged momentum changes are small, the impact on the flow domain was significant. This can be seen in Fig. 4b, which also compares the same OVERFLOW and INS3D simulations by plotting pressure distributions on the tunnel side walls. The side walls correspond to the upper and lower surfaces of the high-lift wing. In Fig. 4b, the lower surface side-wall pressures are essentially equivalent for the OVERFLOW and INS3D solutions prescribing the extrapolation conditions at the tunnel exit. The OVERFLOW solution using the specified mass flow exit condition shows lower pressures on both the lower and upper surface side walls. Moreover, the exit pressure for this case is also lower than the other solutions. Clearly, the specified mass flow exit condition causes a higher flow velocity through the test section region. Note the differences in the upper surface side-wall pressures between the OVERFLOW and INS3D solutions using extrapolation exit conditions in Fig. 4b.

Intuitively, the compressible solutions will show greater suction over the upper surface of the high-lift wing. This compressibility effect is reflected on the upper surface side wall by the lower

pressure distribution for the OVERFLOW solutions through the test section region. The exit condition that prescribes a constant static pressure and extrapolation of other flow variables was used for the OVERFLOW solutions in this study. Although the boundary condition that prescribes a straight extrapolation of all flow variables matches the earlier OVERFLOW extrapolation condition, it slowed convergence in the tunnel zone and, consequently, was not used.

Slat Aerodynamics

Experimental Verification

Computed pressure distributions are compared to experimental data from Ref. 16. All computations for the slat aerodynamic results were run with the OVERFLOW code using a freestream Mach number of 0.22 and the conditions described in the "Numerical Approach" section earlier. For each configuration, two spanwise locations are considered, $y/b = 0.17$ and 0.83. These spanwise locations were chosen for the specific features associated with one-, two-, and three-element flows. All spanwise locations for each configuration showed the same agreement to experiment as the locations shown here. Figures 5, 6, and 7 show the comparisons for the no-slat, full-span slat, and part-span slat wings, respectively. The agreement between computed and experimental pressure coefficients is good for all configurations. Differences occur at the suction peaks of the main element and flap, where the experimental pressure distributions do not have as large a suction peak on the main element as is seen in the computed distributions. The discrepancy occurs in the region where the boundary layer is transitioning from a laminar to turbulent state for the three-element wing configurations and where boundary-layer tripping is occurring on the two-element wing configurations. The lack of transition modeling in the computations will cause discrepancies in these cases. In addition, the influence of the viscous wind-tunnel walls can have an impact on the pressure coefficients, especially at $y/b = 0.83$. In either case, these differences can explain the slight disagreement of the flap suction peak values. Finally, the lower lift on the experimental main element allows the flap to operate at a higher effective angle of attack.

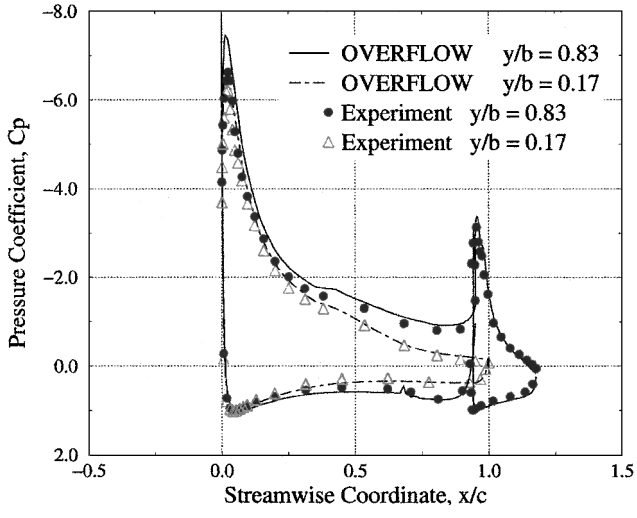

Fig. 5 Comparisons of OVERFLOW computed pressures with experimental measurements[16] at two spanwise locations on the two-element wing, $M_\infty = 0.22$.

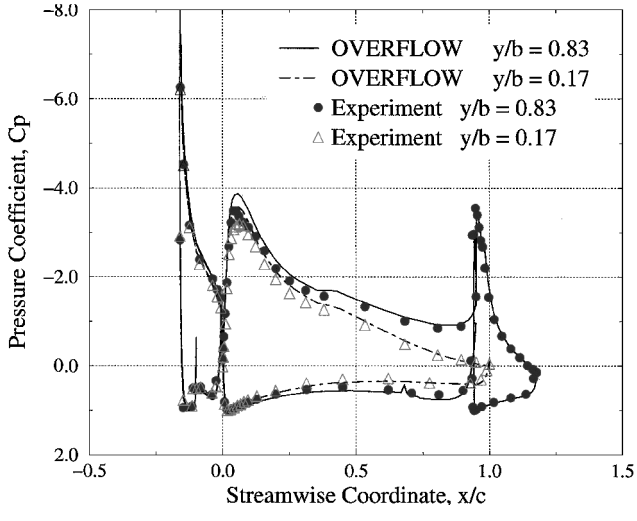

Fig. 6 Comparisons of OVERFLOW computed pressures with experimental measurements[16] at two spanwise locations on the three-element wing with full-span slat, $M_\infty = 0.22$.

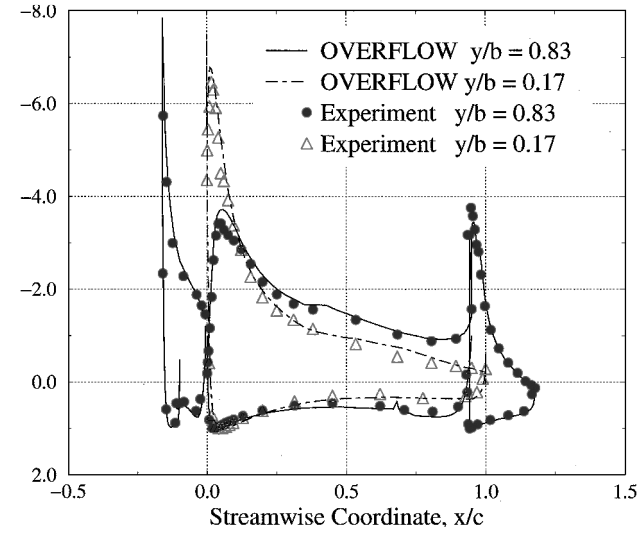

Fig. 7 Comparisons of computed pressures with experimental measurements[16] at two spanwise locations on the three-element wing with part-span slat, $M_\infty = 0.22$.

Slat Flow Features

The flow over the two-element wing has been well documented in the past.[7,8] It is included in this study as a baseline to which the other configurations can be compared. The changes in the flow due to full- and part-span slats can be quantified. Surface particle traces for the two-element wing are shown in Fig. 8a. The particle traces are equivalent to an oil flow pattern for an experiment. The flow on the flapped portion of the main element proceeds in the streamwise direction over most of the span. Near the half-span location, however, there is a tendency for the flow to curve away from the unflapped portion of the wing. This curvature is a result of the velocity induced by the flap-tip vortex. The same effect is seen on the unflapped half of the wing, though to a much larger degree. A large separation line is seen on the unflapped portion of the wing, behind which is a region of reversed flow. A separation line also exists on the flap element near the trailing edge. The surface path lines flow spanwise toward the tip as the flow moves from the lower surface around the tip to the upper surface. This is the flow that results in the tip vortex downstream. By the half-chord point, the vortex is largely formed and induces a velocity toward the tip beneath.

Figure 8b shows a similar view for the full-span slat configuration. The slat causes minor changes in the flow patterns on the surface of the flapped portion of the main element. The separation line on the flap does appear to be shifted aft and even eliminated over about one-half of the flap span. A drastic change in the flow topology is seen on the unflapped main element. The addition of the slat has mitigated the suction peak on the unflapped main element. Reducing the pressure recovery demand on the unflapped portion eliminated the separation region. A general tendency for the particle traces to flow toward the flap tip is still seen. The flow on the upper surface of the slat is nearly streamwise over the entire span.

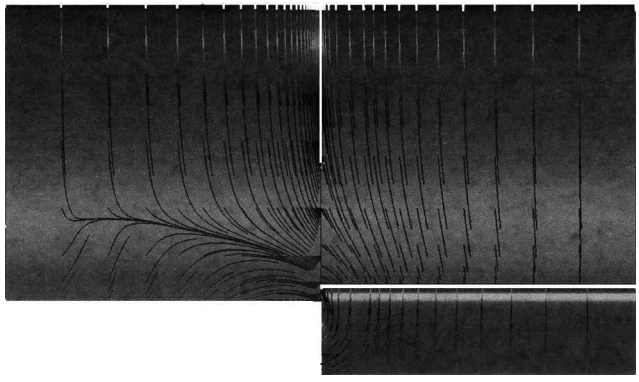

Fig. 8a OVERFLOW computed surface particle traces for the two-element wing, $M_\infty = 0.22$.

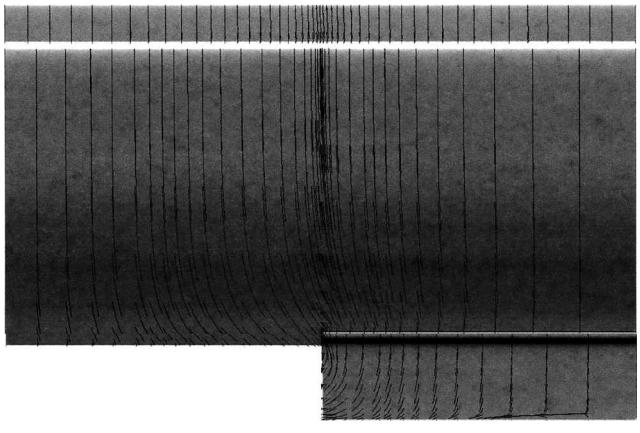

Fig. 8b OVERFLOW computed surface particle traces for the three-element wing with full-span slat, $M_\infty = 0.22$.

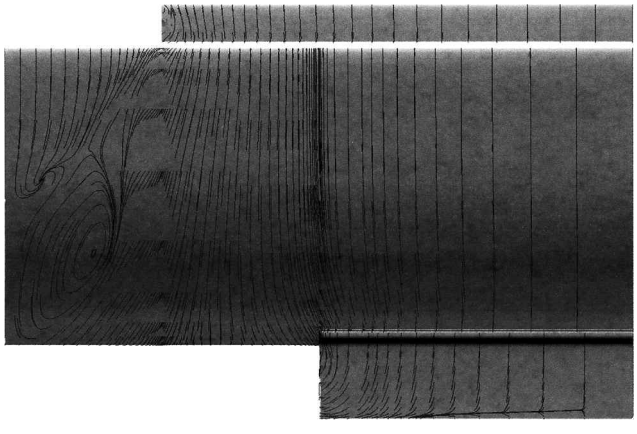

Fig. 8c OVERFLOW computed surface particle traces for the two-element wing with part-span slat, $M_\infty = 0.22$.

Surface particle traces for the part-span slat configuration are shown in Fig. 8c. Particle paths on the flapped main element are still aligned with the freestream. The flow on the flap appears much as it does for the two-element wing. A separation line is present, but is located aft of the two-element separation line and slightly forward of the full-span slat result, and the large change in the flow on the unflapped portion of the wing is visible. A massive separation now exists outboard of the slat tip, and two things are happening to change the flow in this region. First, the slat-tip vortex is adding more upwash over the upper surface of the main element. The upwash is adding to loading on the main element outboard of the slat, causing separation to occur quickly. In addition, the tip vortex from the slat travels above the upper surface of the wing, inducing a flow away from the slat. The long streamwise particle traces resolve this induced path.

Figures 9 show pressure distributions for all three wing configurations at four spanwise locations (Figs. 9a–9d). Table 3 indicates the sectional lift coefficient value of each element of the three wing configurations at the spanwise locations presented. Figure 9a shows the comparison at a y/b location of 0.83 (Fig. 2). At this location, there is roughly 6% difference in slat lift and about 2% in main element lift between the two slat configurations. This is expected because the effects of the slat tip are relatively far removed. The minor differences are a result of the part-span slat carrying slightly less lift than the full-span counterpart due to the slat tip. The lift at the tip disappears, and this is felt over the entire span, though to a small degree at this spanwise location. Note that the upper surface pressures are different only on the main and slat elements. The wing without the slat has a much different pressure distribution. The suction peak at the leading edge of the main element is roughly 75% stronger than the slat cases. This translates into about 18% more lift carried by the main element in the no-slat configuration. All three configurations show the same pressure distributions by about $0.4c$ location. The lower surface pressure levels are nearly the same for all of the wings, though the leading-edge stagnation point moves with the addition of a slat.

The presence of the slat sets up a different flow impingement on the main element leading edge. It actually moves the stagnation point forward slightly. This allows the flow to accelerate over a shorter distance around the leading edge from the stagnation point to the point of maximum suction. Because the flow travels a shorter distance, it accelerates less due to the curvature of the wing section. The result is a weaker suction peak. The flap pressures are similar for all three cases. This is not expected considering the suction difference on the main element. Without the slat, the main element generates more circulation (lift), which, in turn, should induce a greater downwash velocity on the flap. The effect of increased downwash would be to reduce the effective angle of attack of the flap, hence reducing the lift.

Figure 9b contains a similar comparison at a spanwise location of $y/b = 0.502$, which is just inboard of the flap tip. A slightly larger

Table 3 Sectional lift coefficient values for slat aerodynamic study

Element	Configuration	$y/b = 0.83$	$y/b = 0.502$	$y/b = 0.250$	$y/b = 0.170$
Main	No slat	2.655	2.359	2.077	2.040
Flap	No slat	0.380	0.069	N/A	N/A
Slat	Full span	0.611	0.590	0.571	0.567
Main	Full span	2.258	1.992	1.741	1.710
Flap	Full span	0.378	0.031	N/A	N/A
Slat	Part span	0.577	0.542	0.388	N/A
Main	Part span	2.208	1.954	1.977	1.960
Flap	Part span	0.382	0.069	N/A	N/A

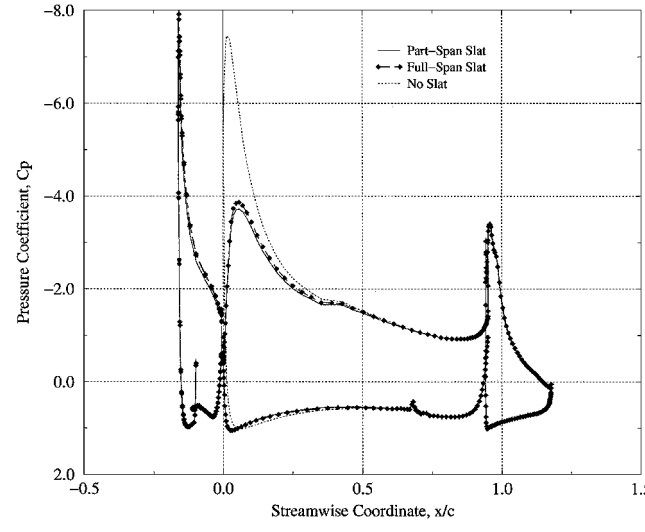

Fig. 9a OVERFLOW computed pressure distributions for the three high-lift wings at spanwise locations, $M_\infty = 0.22$ and $y/b = 0.83$.

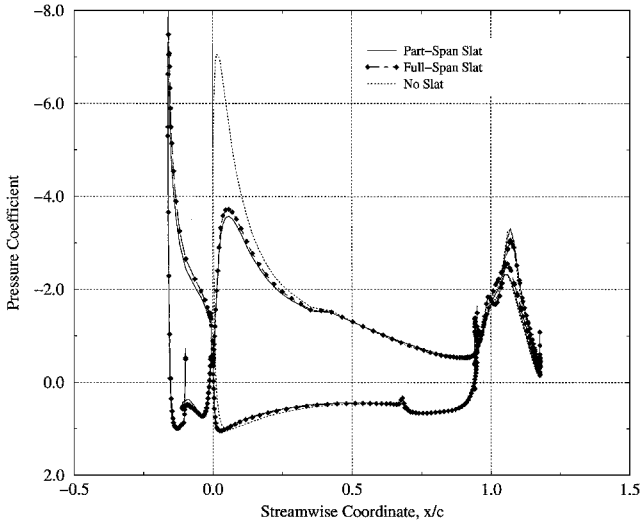

Fig. 9b OVERFLOW computed pressure distributions for the three high-lift wings at spanwise locations, $M_\infty = 0.22$ and $y/b = 0.502$.

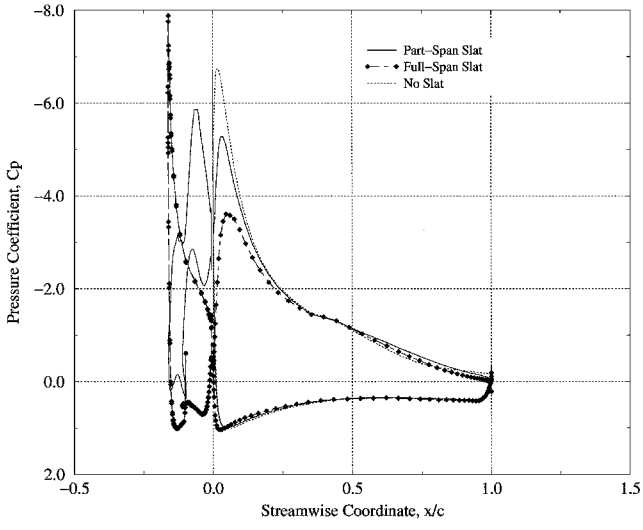

Fig. 9c OVERFLOW computed pressure distributions for the three high-lift wings at spanwise locations, $M_\infty = 0.22$ and $y/b = 0.25$.

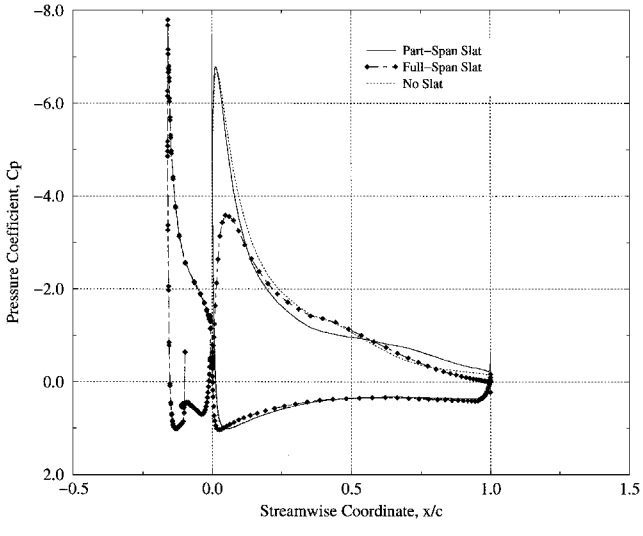

Fig. 9d OVERFLOW computed pressure distributions for the three high-lift wings at spanwise locations, $M_\infty = 0.22$ and $y/b = 0.17$.

difference between the two slat cases is seen on both of the forward two elements compared to Fig. 9a. Again, the lift carried by the two-element wing main element is much larger than that carried by the wings with a slat. The flap lift has dropped off an order of magnitude for all configurations at this location. Although the flap pressures vary significantly, all configurations exhibit a double suction peak on the upper surface of the flap at $y/b = 0.502$.

The double peak is indicative of two separate low-pressure regions. The first peak is the leading-edge suction, although somewhat mitigated by the pressure relief occurring at the tip. The second (or aft) peak is, in all cases, larger than the first and is the result of the tip vortex inducing a large, spanwise velocity between the vortex and the surface. Evidence of the induced flow was seen in Figs. 8a–8c. The magnitude of the first suction peak is roughly the same for all cases, but there are significant differences in the strength of the second peak. The case without the slat is the strongest. Of the other two cases, the part-span slat wing generates a stronger second peak. A very large suction peak is seen on the lower surface of the flap element of each of the wings. The lower surface peaks result from the high spanwise velocities due to the pressure relief at the flap tip.

Figure 9c shows the computed pressure distributions taken just inboard of the slat tip ($y/b = 0.25$). All three of the wings exhibit different characteristics at this point. The full-span slat pressures remain similar to those shown on Figs. 8a and 8b. A 13% difference in lift between the main elements of the part- and full-span slats has been realized. The trends of the pressure distribution at the slat tip are similar to those for the flap tip in Fig. 9b, but the lift only drops off about 40%. A double suction peak exits on the upper surface of the slat, with the aft peak being much stronger. There is also a lower surface suction peak near the slat tip. As the effect of the slat diminishes, the lift on the main element tends toward the value of the no-slat wing. At this location, the part-span slat main element suction is about halfway between the other two wing configurations.

Figure 9d presents a comparison of the three wings outboard of all part-span high-lift elements ($y/b = 0.17$). The pressure distribution for the full-span slat remains roughly the same as before. The suction peaks for the wing sections without a slat at this spanwise location show similar levels of leading-edge suction. However, the large separation region apparent for the part-span slat wing in Fig. 7 is also evident here. The pressure recovery for the part-span slat wing is initially steeper than that of the no-slat wing. This causes the separation that extends over the aft 60% of the chord, as seen by the flat pressure distribution and poor pressure recovery at the trailing edge. The no-slat and full-span slat wings have similar pressure distributions from about $x/c = 0.3$ to near the trailing edge. Also, the stagnation points for the part-span and no-slat sections are at the same location.

Compressibility Effects

Four solution methods listed in Table 2 were implemented for the compressibility study on the three-element wing with part-span slat.[32] The first method used the compressible solution that was described earlier for the slat effects study. Two additional solutions using OVERFLOW were obtained using low Mach preconditioning (LMP) and Mach numbers of 0.22 and 0.001. Finally, a fourth solution was obtained using INS3D, the incompressible solver.

Figure 10 shows the surface pressure distributions on the slat, flapped main, and flap elements at spanwise location $y/b = 0.83$. At this plane, the flow near the surface is largely two dimensional, as seen from the particle traces shown in Fig. 7. Specific lift coefficient values for each element of the four solutions are given in Table 4. Comparison of the two compressible simulations using a

Table 4 Element sectional lift coefficient values at spanwise locations for compressibility effects study, $y/b = 0.83$

Solution	Slat	Main	Flap
OVERFLOW, $M_\infty = 0.22$	0.577	2.208	0.382
OVERFLOW, LMP, $M_\infty = 0.22$	0.576	2.189	0.394
OVERFLOW, LMP, $M_\infty = 0.001$	0.550	2.129	0.397
INS3D	0.515	2.147	0.422

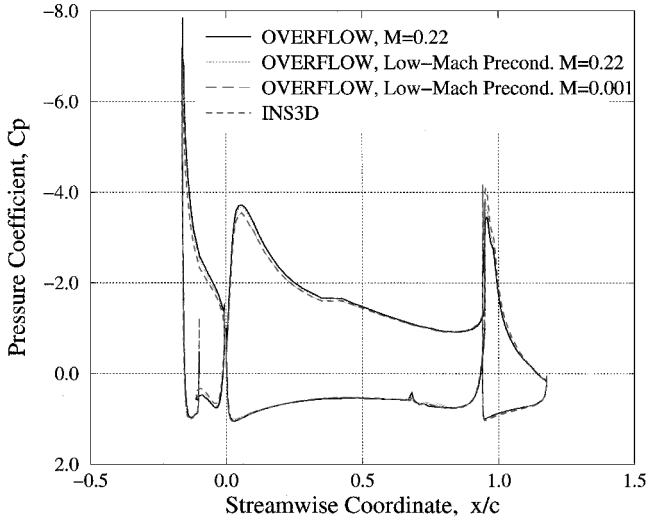

Fig. 10 Pressure distributions for three-element wing with part-span slat at $y/b = 0.83$ for compressible and incompressible simulations.

Mach number of 0.22, but with and without LMP, shows almost no perceptible difference in the computed pressure distributions.

Next, comparison of the OVERFLOW results obtained at a very low Mach number, 0.001, with the results predicted by the incompressible flow solver, INS3D, give confidence in the performance of OVERFLOW for a flow that is essentially incompressible. Remarkably, the pressure distributions of the incompressible solutions are basically equivalent for the flapped main element, the only variation on the flapped main element being in the cove area where the very low Mach number OVERFLOW solution has a slightly lower pressure coefficient. The significant differences between the two solutions appear on the slat and flap elements. The OVERFLOW solution at nearly incompressible conditions predicts slightly more circulation on the slat and slightly less on the flap. One cause for the difference may be due to algorithm differences between the OVERFLOW and INS3D codes. OVERFLOW uses limiters introduced to its spatial discretization scheme to prevent the generation of numerical oscillations, whereas the INS3D implementation does not use limiters. The limiters can also introduce additional levels of artificial dissipation in the solution. The limiters become active at the cusp region of the slat (the sharp edge at the underside of the slat) due to the sharp geometrical discontinuity. The smoothing of the solution in this region changed the velocity condition of the slat and caused the difference in pressure coefficient seen on the upper surface. In turn, the effective change of the slat element circulation contributed to circulation differences on the flap element.

In spite of the impact of the limiters, however, compressibility effects become evident when the compressible and incompressible solution methods are compared; Fig. 10 shows these effects. The differences in suction peaks on the flapped main element between the OVERFLOW solutions computed for Mach numbers of 0.22 and 0.001 show the range of compressibility for this specific high-lift case. The higher suction peak on the main element of the compressible solutions indicate higher circulation and, consequently, smaller suction peak on the flap. Conversely, the lower suction peak on the main element of the incompressible solutions allows for a higher suction peak on the flap.

Figure 11 shows upper surface particle traces from INS3D for the three-element part-span slat wing. Comparing Fig. 11 with Fig. 8c shows that the outboard separation region has become significantly different in the incompressible solution. This separation region is physically unsteady as demonstrated by tuft visualizations during the wind-tunnel test[16]; the steady-state computations also give evidence of this unsteady flow region. The sharp suction peak at leading-edge region of the outboard end of the unflapped main element is increased by the effects of compressibility. A higher velocity in this region puts a greater pressure recovery demand on the main element, causing separation to occur sooner.

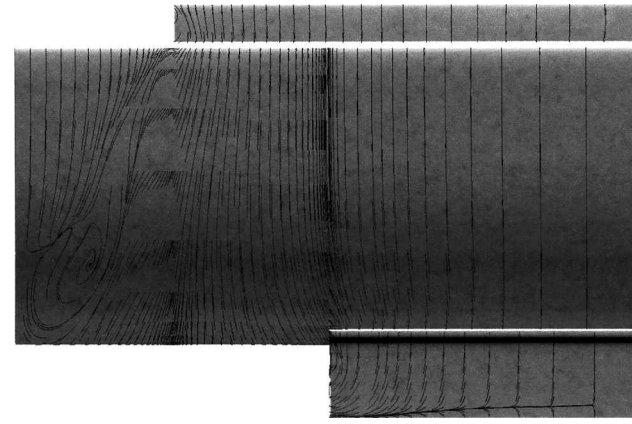

Fig. 11 INS3D surface particle traces for three-element wing with part-span slat.

The separation line on the flap is an important feature that is compared between the OVERFLOW solution in Fig. 8c and the INS3D solution in Fig. 11. The separation line on the flap occurs farthest downstream for the compressible solution and farthest upstream for the incompressible solution. The location of the separation line is due to the strength of the suction peak on the flap leading-edge region. As seen in Figs. 10, the greater loading of the flapped main element due to compressibility causes the flap to further unload and delays separation on the flap; this is an important result. Other researchers have discussed compressibility effects as small and localized to the slat and main element region.[6,33] As seen from Figs. 10 and Table 4, compressibility effects for this three-dimensional high-lift configuration are small, on the order of 2% in total lift coefficient; however, the effects are not local to the slat region. Although compressibility increased the lift on the main element by roughly 3%, the flap element saw a drop in lift by 10%. Moreover, in the case of the outboard separation region, although the compressible zone at the forward tip of the main element is small, separation occurred much sooner, creating a large difference in performance for this portion of the wing.

Conclusions

The flow about an unswept, high-lift wing configured with three different leading-edge devices (no slat, a full-span slat, and a three-quarter span slat) was computed using compressible and incompressible Navier–Stokes solvers on structured overset grid systems. This study extended previous high-lift CFD research on the unswept high-lift wing by adding the slat element. Results for each wing geometry were shown to compare favorably with existing wind-tunnel surface pressure measurements. Examination of computed surface pressure distributions and particle traces for the three high-lift wings verified the fundamental impact of the slat element on the high-lift flowfield. Furthermore, knowledge of the three-dimensional influence of the slat and computational techniques for resolving the flow in the vicinity of a slat tip was gained and will be applied in future simulations.

A basic numerical investigation was conducted by comparing a series of three-dimensional high-lift simulations. It was shown that careful attention must be given to the selection of the inflow/outflow boundary condition specification for CFD simulations of flow within a wind tunnel to achieve similarity with solutions generated by different predictive methods. For this high-lift flow, the simulations validated the LMP algorithm within the OVERFLOW code, as well as the application of the code at incompressible flow conditions. The OVERFLOW and INS3D codes provided an excellent platform for examining compressibility effects due to the similarity in the numerical methods and turbulence model within the codes. The effects due to the small compressible regions of the high-lift flowfield had important global effects. Even though the compressible regions were local to the slat and main element suction peaks, evidence was shown that lift on the flap, as well as separation regions, were significantly altered.

Acknowledgments

This research was supported by NASA Contract Award NCC-2-857. The authors appreciate the helpful suggestions of Stuart E. Rogers of NASA Ames Research Center.

References

[1]Smith, A. M. O., "High-Lift Aerodynamics," AIAA Paper 74-0939, Aug. 1974.

[2]Meredith, P. T., "Viscous Phenomena Affecting High-Lift Systems and Suggestions for Further CFD Development," *Proceedings of the High-Lift System Aerodynamics Conference*, AGARD CP-515, Oct. 1992, pp. 19-1–19-8.

[3]Shuster, D. M., and Birckelbaw, L. D., "Numerical Computation of Viscous Flowfields about Multiple Component Airfoils," AIAA Paper 85-0167, Jan. 1985.

[4]Rumsey, C. L., Gatski, T. B., Ying, S. X., and Bertelrud, A., "Prediction of High-Lift Flows Using Turbulent Closure Models," *AIAA Journal*, Vol. 36, No. 5, 1998, pp. 765–774.

[5]Fejtek, I., "Summary of Code Validation Results for a Multiple Element Airfoil Test Case," AIAA Paper 97-1932, July 1997.

[6]Rogers, S. E., "Progress in High-Lift Aerodynamic Calculations," *Journal of Aircraft*, Vol. 31, No. 6, 1994, pp. 1244–1251.

[7]Mathias, D. L., "Navier–Stokes Analysis of the Flow About a Flap Edge," M.S. Thesis, Aerospace Engineering Dept., California Polytechnic State Univ., San Luis Obispo, CA, June 1994.

[8]Mathias, D. L., Roth, K. R., Ross, J. C., Rogers, S. E., and Cummings, R. M., "Navier–Stokes Analysis of the Flow About a Flap-Edge," *Journal of Aircraft*, Vol. 35, No. 6, 1998, pp. 833–838.

[9]Jones, K. M., Biedron, R. T., and Whitlock, M., "Application of a Navier–Stokes Solver to the Analysis of Multielement Airfoils and Wings Using Multizonal Grid Techniques," AIAA Paper 95-1855, June 1995.

[10]Khorrami, M. R., Singer, B. A., and Takallu, M. A., "Analysis of Flap Side-Edge Flow Field for Identification and Modeling of Possible Noise Sources," *SAE Transactions*, Vol. 106, No. 2, 1997, pp. 2716–2722.

[11]Khorrami, M. R., Singer, B. A., and Radeztsky, R. H., "Reynolds Averaged Navier–Stokes Computations of a Flap Side-Edge Flowfield," *AIAA Journal*, Vol. 37, No. 1, 1999, pp. 14–22.

[12]Mavriplis, D. J., and Venkatakrishnan, V., "A 3-D Agglomeration Multigrid Solver for the Reynolds-Averaged Navier–Stokes Equations on Unstructured Meshes," *International Journal for Numerical Methods in Fluids*, Vol. 23, No. 6, 1996, pp. 527–544.

[13]Anderson, W. K., Rausch, R. D., and Bonhaus, D. L., "Implicit/Multigrid Algorithms for Incompressible Turbulent Flows on Unstructured Grids," *Journal of Computational Physics*, Vol. 128, No. 2, 1996, pp. 391–408.

[14]Rogers, S. E., Cao, H. V., and Su, T. Y., "Grid Generation for Complex High-Lift Configurations," AIAA Paper 98-0311, June 1998.

[15]Hicks, R. M., and Schairer, E. T., "Effects of Upper Surface Modification on the Aerodynamic Characteristics of the NACA 63_2-215 Airfoil Section," NASA TM 78503, 1979.

[16]Storms, B. L., Ross, J. C., Horne, W. C., Hayes, J. A., Dougherty, R. P., Underbrink, J. R., Scharpf, D. F., and Moriarty, P. J., "An Aeroacoustic Study of an Unswept Wing with a Three-Dimensional High-Lift System," NASA TM 112222, Feb. 1998.

[17]Jespersen, D. C., Pulliam, T. H., and Buning, P. G., "Recent Enhancements to OVERFLOW," AIAA Paper 97-0644, Jan. 1997.

[18]Renze, K. J., Buning, P. G., and Rajagopalan, R. G., "A Comparative Study of Turbulence Models for Overset Grids," AIAA Paper 92-0437, Jan. 1992.

[19]Beam, R. M., and Warming, R. F., "An Implicit Factored Scheme for the Compressible Navier–Stokes Equations," *AIAA Journal*, Vol. 16, No. 4, 1978, pp. 393–402.

[20]Pulliam, T. H., and Chaussee, D. S., "A Diagonal Form of an Implicit Approximate Factorization Algorithm," *Journal of Computational Physics*, Vol. 39, No. 2, 1981, pp. 347–363.

[21]Roe, P. L., "Approximate Riemann Solvers, Parameter Vectors, and Difference Schemes," *Journal of Computational Physics*, Vol. 43, No. 2, 1981, pp. 357–372.

[22]Rogers, S. E., "Numerical Solution of the Incompressible Navier–Stokes Equations," NASA TM 102199, Nov. 1990.

[23]Rogers, S. E., Menter, F. R., Durbin, P. A., and Mansour, N. N., "Comparison of Turbulence Models in Computing Multi-Element Airfoil Flows," AIAA Paper 94-0291, Jan. 1994.

[24]Kern, S., "Evaluation of Turbulence Models for High-Lift Military Airfoil Flowfields," AIAA Paper 96-0057, Jan. 1996.

[25]Ying, S. X., "High-Lift: Challenges and Directions for CFD," *Proceedings of the AIAA/NPU Atmospheric Flight Mechanics Conference*, AIAA, Reston, VA, 1996, pp. 164–182.

[26]Spalart, P. R., and Allmaras, S. R., "One-Equation Turbulence Model for Aerodynamic Flows," AIAA Paper 92-0439, Jan. 1992.

[27]Chan, W. M., Nash, S., Buning, P. G., and Rogers, S. E., "Chimera Grid Tools, Version 0.4," NASA Ames Research Center, Moffett Field, CA, Feb. 1998.

[28]Chan, W. M., Chiu, I. T., and Buning, P. G., "User's Manual for the HYPGEN Hyperbolic Grid Generator and the HGUI Graphical User Interface," NASA TM 108791, Oct. 1993.

[29]Baker, M. D., Mathias, D. L., Roth, K. R., and Cummings, R. M., "Numerical Investigation of Slat and Compressibility Effects for a High-Lift Wing," AIAA Paper 99-0538, Jan. 1999.

[30]Tramel, R. W., and Suhs, N. E., "PEGSUS 4.0 User's Manual," Arnold Engineering Development Center, Arnold AFB, TN AEDC TR-91-8, June 1991.

[31]Djomehri, M. J., "CFD Modeling of the 12-Foot Pressure Wind Tunnel," Calspan SRL Corp., Final Rept., Moffett Field, CA, Apr. 1996.

[32]Baker, M. D., "Numerical Investigation of Compressibility Effects in Low-Speed, Low-Reynolds Number High-Lift Flows," M.S. Thesis, Aerospace Engineering Dept., California Polytechnic State Univ., San Luis Obispo, CA, June 1998.

[33]Woodward, D. S., Hardy, B. C., and Ashill, P. R., "Some Types of Scale Effects in Low-Speed, High-Lift Flows," *Proceedings of the 16th ICAS Congress*, AIAA, New York, 1988, pp. 1402–1416.